AGU100 ADVANCING EARTH AND SPACE SCIENCE

Water Resources Research

RESEARCH ARTICLE

10.1029/2019WR026060

Key Points:
- A modified stream function formulation for multicomponent reactive convective-diffusive CO_2 mixing is presented
- Temporal and spatial dependency of geochemical effects in CO_2 mixing and sequestration was studied
- Solubility trapping and carbon mineralization alter significantly with Rayleigh number

Supporting Information:
- Supporting Information S1

Correspondence to:
V. Niasar,
vahid.niasar@manchester.ac.uk

Citation:
Erfani, H., Babaei, M., & Niasar, V. (2020). Signature of geochemistry on density-driven CO_2 mixing in sandstone aquifers. *Water Resources Research*, *56*, e2019WR026060. https://doi.org/10.1029/2019WR026060

Received 27 JUL 2019
Accepted 19 FEB 2020
Accepted article online 21 FEB 2020

Signature of Geochemistry on Density-Driven CO_2 Mixing in Sandstone Aquifers

Hamidreza Erfani[1], Masoud Babaei[1], and Vahid Niasar[1]

[1]Department of Chemical Engineering and Analytical Science, University of Manchester, Manchester, UK

Abstract Density-driven mixing resulting from CO_2 injection into aquifers leads to the CO_2 entrapment mechanism of solubility trapping. Crucially, the coupled flow-geochemistry and effects of geochemistry on density-driven mixing process for "sandstone rocks" have not been adequately addressed. Often, there are conflicting remarks in the literature as to whether geochemistry promotes or undermines dissolution-driven convection in sandstone aquifers. Against this backdrop, we simulate density-driven mixing in sandstone aquifers by developing a 2-D modified stream function formulation for multicomponent reactive convective-diffusive CO_2 mixing. Two different cases corresponding to laboratory and field scales are studied to investigate the effect of rock-fluid interaction on density-driven mixing and the role of mineralization in carbon storage over the project life time. A complex sandstone mineralogical assemblage is considered, and solid-phase reactions are assumed to be kinetic to study the length- and time-scale dependency of the geochemistry effects. The study revealed nonuniform impact of rock-fluid and fluid-fluid interaction in early- and late-time stages of the process. The results show that for moderate Rayleigh (Ra) numbers, rock-fluid interactions adversely affect solubility trapping while improving the total carbon captured through mineral trapping. Simulation results in the range of $1{,}500 < Ra < 55{,}000$ in the field-scale model showed more pronounced impact of geochemistry for higher Ra numbers, as geochemistry stimulates the convective instabilities and improves the total sequestered carbon. This study gives new insights into the effect of rock-fluid interactions on density-driven mixing and solubility trapping in sandstone aquifers to improve estimation of the carbon storage capacity in deep saline aquifers.

1. Introduction

1.1. Background and Gaps

Greenhouse gases are major reason for global warming and climate change (Oreskes, 2004). Among greenhouse gases, CO_2 is responsible for two third of the global warming caused by human activities (Rogelj et al., 2016). The level of carbon emission to the atmosphere must be decreased significantly to avoid detrimental global climate change. To this end, more than 190 countries have agreed in the Paris agreement to keep the global average temperature increase below 2 ° C as a long-term goal (Judith, 2017). For this purpose, almost 20 Gt CO_2/year must be captured and stored to reach zero net carbon emission (Majumdar & Deutch, 2018; Orr Jr, 2018).

Carbon capture and storage (CCS) is the only available technology that allows a continued use of fossil fuels while addressing the carbon emission problem (Bui et al., 2018; Celia, 2017; Haszeldine, 2009). In this technology, CO_2 is captured from anthropogenic sources before being emitted to the atmosphere and then injected in deep saline aquifers, depleted oil and gas reservoirs or geological traps (Edwards et al., 2015; Rockström et al., 2016). During such processes, CO_2 trapping mechanisms of structural trapping, residual trapping, solubility trapping, and mineralization (Aminu et al., 2017; Bakhshi et al., 2018; Balashov et al., 2013; Kampman et al., 2014; Joekar-Niasar et al., 2013) can occur. The available storage capacity in deep saline aquifers is estimated to be roughly 2 orders of magnitude greater than the capacity in depleted oil and gas reservoirs. As an example, in the case of the United States the CO_2 storage capacity for saline aquifers is estimated as 12,000 Gt CO_2 (Celia, 2017) while the estimation for depleted oil reservoirs is about 20 Gt CO_2 (Godec et al., 2011). So deep saline aquifers are the primary long-term options for carbon problem mitigation, while in the near-term CO_2-enhanced oil recovery (EOR) is increasingly being recognized as a commercial alternative to storage only operations (Balashov et al., 2013; Koytsoumpa et al., 2017; Kolster et al., 2017; Orr Jr, 2009; Shokri et al., 2018; Tapia et al., 2016).

CO_2 is usually injected in supercritical (SC) state, which is less dense and less viscous than the native fluid. Consequently, CO_2 overrides to the top of the formation. Once CO_2 reaches the impermeable caprock, it will initially remain in the aquifer as a separate phase but will eventually dissolve into the aqueous phase. This results in a denser aqueous phase, and an instability is created by a denser phase being on the top of a less dense native fluid. This instability promotes CO_2 spreading into the aquifer through convective-diffusive mixing, which brings CO_2-rich aqueous phase downward and creates finger-shape CO_2 concentration profiles (Amooie et al., 2018; Balashov et al., 2013; Ennis-King & Paterson, 2007; Farajzadeh et al., 2007; Loodts et al., 2017; Orr Jr, 2009; Sainz-Garcia et al., 2017).

CO_2 dissolution is a key parameter in CCS, as it increases the storage security by promoting CO_2-rock interactions, which may result in carbon mineralization (Audigane et al., 2007; Emami-Meybodi & Hassanzadeh, 2015; Hassanzadeh et al., 2007; Moghaddam et al., 2012). Sathaye et al. (2014) used real-life data of a natural analog for geological CO_2 storage and concluded that convection-diffusion is taking place in that field. Different researchers have studied convective mixing in saline aquifers by experiments (Agartan et al., 2015; Cardoso & Andres, 2014; Cinar et al., 2007; Moghaddam et al., 2012), and different numerical schemes, mostly focusing on the onset of the instability and convection, the effect of permeability heterogeneity, and aquifer natural flow (Audigane et al., 2007; Amooie et al., 2018; Ghesmat et al., 2011; Meybodi & Hassanzadeh, 2013; Soltanian et al., 2017; White et al., 2005; Yang et al., 2015), were developed. Although experimental quantification of fluid-rock interaction effects on CO_2 convection-dissolution processes is difficult, some modeling approaches have been followed by different researchers in this area of research (Balashov et al., 2013; Babaei & Islam, 2018; Fu et al., 2015; Hidalgo et al., 2015; Islam et al., 2016; Kampman et al., 2014; Liu et al., 2011; Sainz-Garcia et al., 2017). However, none of these studies addresses the effects of geochemistry of *sandstone rocks* on the convection-diffusion process.

Fu et al. (2015) and Hidalgo et al. (2015) simulated density-driven convection in carbonate aquifers using mixing-ratio-based reactive transport modeling. They showed that the porosity increase due to the geochemical reactions is almost 8% and occurs mostly at the thin top domain interface, which helps the process through CO_2 flux increase. Islam et al. (2016) coupled a geochemistry solver for carbonate aquifers from De Simoni et al. (2007), with the hydrodynamics of flow (solute transport solver). Using this method, they found that the porosity and permeability changes (0.06%) are negligible and do not affect the hydrodynamics at all. However, the changes in local concentrations substantially enhance the density-driven convection. Sainz-Garcia et al. (2017) used iCP interface (Nardi et al., 2014) to couple COMSOL (Multiphysics & COMSOL, 2012) and PHREEQC (Charlton & Parkhurst, 2011) geochemical modules to model the kinetics of the carbonate rock-CO_2 interactions during density-driven flow in aquifers. They concluded that the geochemical interactions enhance the instability and stimulate the convection onset.

Even though the dynamics of aqueous CO_2-sandstone rocks at the field scale were investigated by many researchers (Amin et al., 2014; Audigane et al., 2007; Knauss et al., 2005; Soltanian et al., 2019; White et al., 2005; Xu et al., 2005), none of them focused on density-driven mixing and the impact of rock-fluid interaction on the phenomenon. Notably, all of the studies mentioned above have reported positive overall impact of the geochemical interactions on the amount of captured CO_2 in long term. The work by Cardoso and Andres (2014) is one of the few publications that reports (based on experimental results) that in low Rayleigh (Ra) numbers, the geochemical interactions may hinder CO_2 natural convection in silicate-rich rocks. They have used methyl isobutyl ketone (MIBK) and aqueous solution of sodium hydroxide as sample rock and fluid system in Hele-Shaw cell experiments. The reactions were assumed to continue indefinitely, whereas in most geological situations, possible reactions are limited by the finite amount of reactants available in any specific volume of the pore space (Emami-Meybodi et al., 2015).

In this research, PhreeqcRM (Charlton & Parkhurst, 2011; Parkhurst & Wissmeier, 2015) is coupled with a multicomponent convection-diffusion simulator to study the effect of geochemistry on density-driven mixing during carbon storage in sandstone aquifers. Four primary minerals (quartz, albite, k-feldspar, and dolomite) along with four secondary minerals (kaolinite, dawsonite, calcite, and magnesite) are considered in the model to obtain a realistic sandstone geochemical representation. Ten aqueous-phase equilibrium reactions are solved along with above-mentioned solid-phase (mineral) reactions to specify species interactions in the aqueous phase. This study explores the effect of rock-fluid interactions in sandstone aquifers with a focus on convective-diffusive region, placed far from the injection well, where gravity override has driven SC CO_2 to the top of the aquifer.

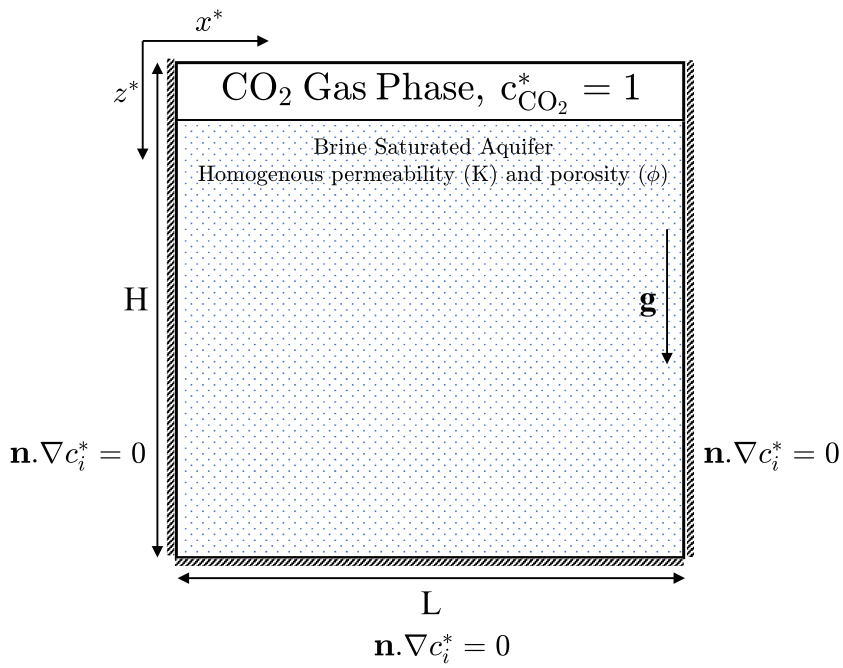

Figure 1. Schematic diagram of the simulation domain and the boundary conditions (**n** is normal unit vector toward the surface.).

1.2. Objectives

We aim to address the following fundamental research questions:

- How does geochemistry influence convective-diffusive mixing and mineralization in sandstone formations?
- What is the length- and time-scale dependency of sandstone geochemical reactions on density-driven mixing?
- What is the impact of the geochemical interactions on the onset of convective mixing and rock mineral alteration during CO_2 sequestration in sandstone aquifers?

This study has three main features, which make it distinct from other numerical studies of this field. First of all, existing stream function formulation is modified to incorporate multicomponent reactive convective-diffusive mixing. For this purpose, different species are lumped into pseudo-components; then the effect of different pseudo-components concentration change on the density and mixing are combined with the stream function formulation. Second, the details of rock-fluid and fluid-fluid interactions are presented through considering a complex assemblage of geochemical reactions representative for sandstone aquifers. Third, time- and length-scale dependency of the geochemical effect are delineated for early- and late-time stages of the process.

In the remainder of the paper, first, the simulation domain and the problem are described and the governing equations are presented. Then, the rate equation for kinetic reactions is reviewed briefly, and all involved geochemical reactions for the sandstone rock interactions with CO_2 are presented. Next, the numerical methods and the physical characteristics of the simulation domain are explained. In the results and discussion section, the simulation results are provided and are compared with no-reaction simulation. Finally, the conclusions from simulation results and their implications in CCS are presented.

2. Methodology

2.1. Problem Description and Governing Equations

A two-dimensional rectangular domain, representing an isothermal aquifer saturated with brine with height H and length L (see Figure 1) is considered. Initially, the fluid is in chemical equilibrium with rock constituents (primary minerals) at the reservoir temperature. All boundaries of the domain are closed, and additional assumptions are as follows:

- CO_2-brine interface is sharp and fixed at the top boundary position.
- The pressure change due to dissolution is negligible (Ennis-King & Paterson, 2005; Islam et al., 2013).
- Gaseous CO_2 has no interaction with rock (Balashov et al., 2013; Gaus, 2010).
- Permeability (K) field is homogeneous and isotropic. Porosity (ϕ) and rock mineral composition are homogeneous as well.
- Rock dissolution/precipitation does not change rock properties, but the porosity and permeability changes are calculated at the end of the simulation.
- The Boussinesq approximation and Darcy's law are assumed to be valid, convective flow does not generate large flow velocities, and flow is assumed to be laminar (Nield & Bejan, 2006)
- Impact of velocity on dispersion of CO_2 is neglected.

The governing equations of flow and transport of species are as follows:

a. continuity equation

$$\phi \frac{\partial \rho}{\partial t} + \frac{\partial(\rho u_x)}{\partial x} + \frac{\partial\left(\rho u_z\right)}{\partial z} = 0, \tag{1}$$

b. Darcy's law

$$u_x = -\frac{K}{\mu}\frac{\partial p}{\partial x} \quad , \quad u_z = -\frac{K}{\mu}\left(\frac{\partial p}{\partial z} - \rho g\right), \tag{2}$$

c. reactive transport of chemical species

$$\phi\ \frac{\partial c_i}{\partial t} + \frac{\partial(u_x\ c_i)}{\partial x} + \frac{\partial(u_z\ c_i)}{\partial z} = \phi D_i\left(\frac{\partial^2 c_i}{\partial x^2} + \frac{\partial^2 c_i}{\partial z^2}\right) + \underbrace{S_i}_{\text{Reaction}}, \tag{3}$$

where D_i is diffusion coefficient and S_i $\left[\text{mol}\ \ \text{kg}_\text{w}^{-1}\ \ \text{s}^{-1}\right]$ denotes the sink/source term of the species i due to the geochemical reactions. We solve advection-diffusion equation in our system, as initially, there is no velocity in the domain. By diffusion of dissolved CO_2 in water and gradual increase of density, the convection (advection) will trigger which would lead to development of the velocity field and potential dispersion of the dissolved CO_2. Some researchers have concluded that dispersion might enhance the fingering in the this context (Chevalier et al., 2015; Hidalgo & Carrera, 2009). However, since the stream functions we provide will be significantly more complex that the current form and also the focus of the paper is to delineate the impact of the geochemistry versus the no-reaction case, we analyzed the convection-diffusion in our formulations.

d. Density change due to concentration

$$\rho = \rho_0\ \left[1 + \sum_{n=1}^{n_s}\beta_i\ (c_i - c_{0,i})\right], \tag{4}$$

where $c_{i,0}$ denotes the initial concentration of the species i and β_i is defined as

$$\beta_i = \frac{1}{\rho_0}\left[\frac{\partial\ \rho}{\partial c_i}\right]_{T,c_{j\neq i}}. \tag{5}$$

If we define a reference coefficient of density increase by concentration, β_r, for one of the species (usually CO_2 as it has the highest impact on fluid density due to its high concentration) and write equation (4) in differential form, we have

$$\frac{\partial \rho}{\partial x} = \rho_0\ \beta_r\left[\sum_{i=1}^{n_s}\frac{\beta_i}{\beta_r}\frac{\partial c_i}{\partial x}\right]. \tag{6}$$

After eliminating the pressure by cross-differentiation of equation (2), we get

$$\frac{\partial u_z}{\partial x} - \frac{\partial u_x}{\partial z} = \frac{Kg\rho_0\beta_r}{\mu}\left[\sum_{i=1}^{n_s}\frac{\beta_i}{\beta_r}\frac{\partial c_i}{\partial x}\right]. \tag{7}$$

So in dimensional form, equations (1), (3), (6) and (7) must be solved for variables of velocity (u_x and u_z) and concentration fields.

2.2. Dimensionless Pseudo-Component Stream Functions

In order to take into account the density difference due to concentration change, we can lump different species with the same element into a pseudo-species concentration $\left(\text{i.e.,}\quad \widehat{C_c} = c_{CO_2} + c_{HCO_3^-} + c_{CaHCO_3^+} + c_{MgHCO_3^+} + c_{CO_2} + c_{CO_3^{-2}}\right)$. For the purpose of writing equations in dimensionless form, the dimensionless concentration can be defined as $c_i^* = \frac{c_i - c_{i,0}}{c_{i,r} - c_{i,0}}$, where $c_{i,r}$ and $c_{i,0}$ denote the reference (top boundary) and initial concentration of the species i, respectively. We also need to define the corresponding effective diffusion coefficient for each pseudo-component ($\widehat{D_{ps}}$) (Li et al., 2006; Sainz-Garcia et al., 2017), as well as the coefficient of density change ($\widehat{\beta}$), which is defined the same as equation (5) for each pseudo-component and can be calculated in the same way as $\widehat{D}$.

$$\widehat{D_{ps}} = \frac{\sum_{i=1}^{n} c_i^* D_i}{\sum_{i=1}^{n} c_i^*} \tag{8}$$

We also need a reference diffusion coefficient $\left(D_r\right)$ in order to calculate Ra number, which is defined based on carbon pseudo-component at the upper boundary as

$$\widehat{D_{c,r}} = \frac{\sum_{i=1}^{n} c_{i,r}^* D_i}{\sum_{i=1}^{n} c_{i,r}^*}, \tag{9}$$

where n is defined as the number of species in the pseudo-component for which the diffusion coefficient is being calculated. The subscript c in equation (9) stands for carbon pseudo-component. As a result, we can define Rayleigh number as

$$Ra = \frac{\Delta\rho\, g K_0 H}{\phi D \mu} = \frac{\rho_0 \widehat{\beta}_c (\Delta \widehat{C_c}) g K_0 H}{\phi \widehat{D_{c,r}} \mu}. \tag{10}$$

Dimensionless variables are defined as

$$x^* = x/L,\ z^* = z/H,\ u_x^* = \frac{L u_x}{\phi D_r},\ u_z^* = \frac{H u_z}{\phi D_r},\ \psi^* = \frac{\psi}{\phi D_r},\ t^* = \frac{D_r t}{H^2},$$
$$\beta^* = \frac{\beta}{\widehat{\beta}_c},\ D^* = \frac{D}{\widehat{D_c}},\ u_x = -\frac{\partial \psi}{\partial z},\ u_z = \frac{\partial \psi}{\partial x},\ \chi = \frac{H}{L}.$$

Then we can write equation (6) in the dimensionless form as

$$\frac{\partial^2 \psi^*}{\partial x^{*2}} + \frac{1}{\chi^2}\frac{\partial^2 \psi^*}{\partial z^{*2}} = \frac{1}{\chi} Ra \left(\sum_{i=1}^{n_{ps}} \frac{\widehat{\beta}_i^* \Delta \widehat{C}_i}{\Delta \widehat{C_c}} \frac{\partial \widehat{C_i^*}}{\partial x^*} \right), \tag{11}$$

where n_{ps} denotes the number of pseudo-components. In this paper we considered simulation domains with equal height and length ($\chi = 1$). For each species, the dimensionless convection-diffusion reactive partial differential equation reads as

$$\frac{\partial c_i^*}{\partial t^*} + \frac{\partial (u_x^* c_i^*)}{\partial x^*} + \frac{\partial (u_z^* c_i^*)}{\partial z^*} = D_i^* \left(\frac{\partial^2 c_i^*}{\partial x^{*2}} + \frac{\partial^2 c_i^*}{\partial z^{*2}} \right) + \underbrace{S_i^*}_{\text{Reaction}}. \tag{12}$$

2.3. Geochemistry

In this work, geochemistry is modeled by coupling PhreeqcRM (Charlton & Parkhurst, 2011; Parkhurst & Wissmeier, 2015) with an in-house convective-diffusive transport simulator. Geochemical reactions are coupled with flow equations by sequential noniterative approach (SNIA) (Barry et al., 2000; Charlton & Parkhurst, 2011; Carrayrou et al., 2004; Erfani et al., 2019; Farajzadeh et al., 2012; Kanney et al., 2003).

Solid-phase reactions are considered as kinetic reactions, and aqueous-phase reactions are assumed to proceed instantaneously (equilibrium condition). The general form of kinetic (solid-phase) reactions can be written as

$$\frac{dm_i}{dt} = \mathscr{A}_i \left(k_{\mathrm{H}}\{\mathrm{H}^+\}^{n_1} + k_{\mathrm{H}_2O} + k_{\mathrm{OH}}\{\mathrm{OH}^-\}^{n_2}\right)\left(1 - \Omega_i^m\right), \tag{13}$$

where $\mathscr{A}_i$ is the reactive surface area of the mineral i and Ω is the saturation ratio, defined as the ratio of Ionic Activity Product (IAP) to equilibrium reaction constant (K_{eq}). Note that the third reaction rate term $\left(K_{\mathrm{OH}}\{\mathrm{OH}^-\}^{n_2}\right)$ is replaced by carbonate mechanism for carbonate minerals (Palandri & Kharaka, 2004). The rate coefficients and powers are taken from the literature (Palandri & Kharaka, 2004, and references cited therein) and adjusted to the simulation temperature using the Arrhenius equation (Laidler, 1984). Moreover, reaction equilibrium constants are taken from literature, and temperature dependency is considered by the analytical five-term formulation or Arrhenius equation, in case the analytical coefficients were not available (Blanc et al., 2012; Parkhurst & Appelo, 1999).

In this research, four primary minerals (quartz, k-feldspar, albite, and dolomite) along with four secondary minerals (calcite, magnesite, dawsonite, and kaolinite) are considered. All mineral reactions, aqueous-phase reactions, and their equilibrium constants at 298.15 K are presented in Table S1 in the supporting information. In brief, eight solid-phase kinetic reactions as well as 10 aqueous-phase equilibrium reactions are considered to model rock-fluid interactions. Solving all chemical reactions presented in Table S1 gives the change of each species as well as the amount of mineral dissolution/precipitation over a time step, which can be related to the change of concentration in equation (3) using the pore volume of the grid block and water density $\left(\frac{dm_i}{dt} \times \frac{1}{\rho_w \phi V_b} = \frac{dc_i}{dt}\right)$.

The surface area of rock, $\mathscr{A}$, is estimated based on modified Kozeny-Carman (Xu & Yu, 2008) equation using porosity and permeability:

$$\mathscr{A} = V_b\left(\frac{\phi_0^3}{5 \times K\left(1 - \phi_0\right)^2}\right)^{0.5}. \tag{14}$$

Also, the porosity (ϕ) for each grid block can be calculated at the end of simulation according to

$$\phi_i^t = \phi_0 - \frac{1}{V_b}\sum_{t=0}^{t}\sum_{n=1}^{np} \pm d_{n,i}^t V_{m,n}, \tag{15}$$

where ϕ_0 is initial porosity, t is time, V_b $\left(\mathrm{m}^3\right)$ is the block pore volume, np denotes total number of minerals, $d_{n,i}$ (mol) denotes the amount of precipitation/dissolution for the nth phase in ith block, and $V_{m,n}$ $\left(\mathrm{m}^3 \quad \mathrm{mol}^{-1}\right)$ is the molar volume of the nth mineral.

In each time step, the amount of mineral trapping carbon, in mole, is calculated as

$$C_{\mathrm{mineralized}}(t) = \sum_{t=0}^{t}\left(2 \times d_{\mathrm{dolomite}}^t + d_{\mathrm{dawsonite}}^t + d_{\mathrm{calcite}}^t + d_{\mathrm{magnesite}}^t\right). \tag{16}$$

The amount of carbon solubility trapping is calculated by multiplying aquifer pore volume by average carbon pseudo-component concentration $\left(\widehat{C_c}\right)$:

$$C_{\mathrm{solubility}}(t) = \int_0^{x=L}\int_0^{z=H} \widehat{C_c}(x, z, t)\, \phi\, dxdz, \tag{17}$$

and the total sequestered carbon will be the summation of solubility and mineral trapping.

3. Materials and Methods

To simulate the convective-diffusive CO_2 transport process in each time step, equation (11) must be solved over the simulation domain to calculate stream function (ψ^*) and extract velocity $\left(u_x^*, u_z^*\right)$ maps in the dimensionless domain. Then, to obtain the dimensionless concentration $\left(c_i^*\right)$ map of each species over the field, equation (12) (excluding the reaction term) must be solved separately for each species. Next, the

dimensionless concentrations are converted into the dimensional form, and the geochemistry term is solved over the dimensional time to update the concentrations. Equation (11) is a 2-D Poisson partial differential equation and was solved using discrete Fourier transform (DFT) (Cooley et al., 1970; Schumann & Sweet, 1988) method while equation (12) was solved by the forward-time central-space (FTCS) method (Kurtz et al., 1978). FTCS is a finite difference scheme with implicit Euler time integration (forward-time) and a central scheme for space discretization (central-space).

To study the effect of geochemical reactions on convective-diffusive mixing in sandstone aquifers, two reactive models are simulated:

1. Laboratory-scale model, 1 m × 1 m dimension (hereafter referred to as the Case 1).
2. Field-scale model, 50 m × 50 m dimension (hereafter referred to as the Case 2).

Investigation of two different physical scales allows us to study length- and time-scale dependency of the geochemical effects on the convection-diffusion process. Additionally, the laboratory-scale case gives us a good insight about the early time mechanisms in the field scale. These cases are also simulated in nonreactive situations to make a comparison between reactive and nonreactive conditions. We chose 50 times bigger domain to makes a significant difference to emphasis the difference between these two domains. Also, due to the coupling scheme as well as kinetic modeling of the geochemical reactions, the time step should be reasonably small to guarantee the numerical convergence and accuracy.

Dimensionless time step was set to 10^{-6}, to guarantee the convergence of FCTS as well as the accuracy of SNIA coupling of geochemistry with hydrodynamics. We have studied the effect of time stepping on results (not reported here for sake of brevity), with 10 times and 100 times smaller time steps, which did not significantly change the results. The dimensionless time step corresponds to the dimensional time step of ≈300 s and ≈10 days for laboratory- and field-scale cases, respectively. In order to develop finger-like front propagation, the CO_2-water interface concentration needs to be perturbed. For this purpose, random numbers were generated as $c^*_{CO_2} = (0.985, 1.015)$, while the boundary condition was kept the same in all simulations to be able to make a comparison. The coefficient of density change (equation (5)) for different pseudo-components were calculated by matching a line on the plot of density versus component concentration, obtained from PHREEQC output, in the simulation pressure and temperature. Diffusion coefficients of different species for different temperatures were taken from the literature (Cussler, 2009; Lasaga, 2014) and extrapolated to the simulation temperature. Initial water composition and reservoir temperature were taken from Xu et al. (2005); mineral selection was taken after Liu et al. (2011) (Table S2). The composition of equilibrated water with rock minerals at the simulation temperature is presented in Table S3 . Initial aquifer porosity was set as $\phi = 0.15$. For laboratory- and field-scale models, the transmissivity was kept constant $\left(KH = 5 \times 10^{-12}\ \mathrm{m}^3\right)$, to obtain the same Rayleigh (equation (10)) number for a comparison study, while in section 4.4 the Rayleigh was controlled by changing the domain permeability and keeping the height constant. To calculate the amount of precipitated mineral using equation (13), a surface area must be associated with that mineral, on which the mineral is precipitating. To overcome this issue, we assigned 10% of the total rock surface to the mineral precipitation (Gaus et al., 2005; Hellevang et al., 2013). The developed code (in the no-reaction condition) was checked against published results (Hassanzadeh et al., 2005; Hidalgo & Carrera, 2009; Islam et al., 2013; Sainz-Garcia et al., 2017), and a satisfactory match was obtained.

4. Results and Discussion

In this section we investigate the reactive density-driven CO_2 mixing in sandstone aquifers. First of all, no-reaction case is presented to clarify the dynamics of convective-diffusive transport. In section 4.2 the role of geochemical reactions are studied at two different scales. Noteworthy, the laboratory-scale simulation results give a good insight about the involving mechanisms in the early time in the field scale. For this purpose, the amount of sequestered CO_2 and the role of mineral trapping are studied for both cases. In section 4.3, carbon trapping mechanism is studied under consideration of rock-fluid interactions, which clarifies why the solubility trapping increases in laboratory scale (or alternatively at early time in the field scale), while it decreases in the field scale. The contribution of mineral dissolution and precipitation at different regions of the CO_2 plumes are studied to shed light on the underlying phenomena. Finally, the effect of geochemical reactions on total sequestered carbon, convection onset time, and plume downward migration in the field scale is studied at different *Ra* numbers.

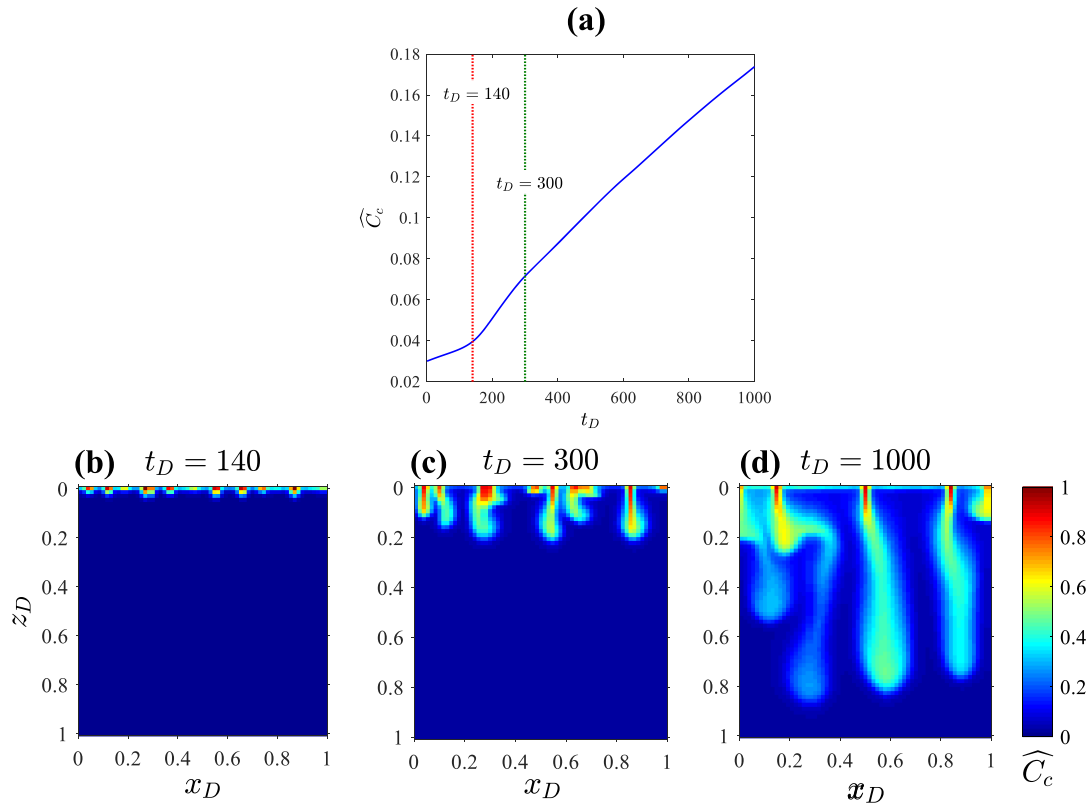

Figure 2. Average dimensionless concentration of carbon pseudo-component versus dimensionless time (a) and dimensionless carbon pseudo-component concentration profile for three different time snapshots for nonreactive case (b-d).

4.1. Convective-Diffusive Mixing (Base Case)

This subsection provides the results of the base case (no reactive flow). Since the base case is nonreactive, it is simulated in the dimensionless domain, and the results are presented based on the dimensionless variables as well. As the process starts, CO_2 penetrates into the aquifer by diffusion, which increases the density in the diffusive layer and triggers instability. The instability results in convective mixing and formation of CO_2 concentration plumes/fingers. With time, the fingers penetrate deeper in the aquifer and merge with each other to form bigger fingers. The native aquifer fluid (less dense) moves upward, while the CO_2-rich fluid migrates downward. When the diffusive layer is ruptured and the native fluid reaches the upper boundary, the horizontal movements of native fluid help the fingers to join each other and form bigger plumes. Figure 2a shows the average concentration of carbon pseudo-component in the simulation domain versus dimensionless time (which associates with different time scales based on the domain size, as $t = \frac{t_D H^2}{D_r}$). Two different time snapshots are marked on Figure 2a, and the corresponding concentration profiles are presented in Figures 2b–2d.

The nonreactive case was simulated in dimensionless domain, while the kinetic geochemistry should be solved in the dimensional domain for the reactive simulation cases. As was mentioned in section 3, two cases with different scales are considered. Cases 1 and 2 correspond to laboratory scale and field scale, respectively. In these cases carbon is sequestered due to both mineral and solubility trapping mechanisms. To be able to draw a comparison between different cases, the results are presented as moles of sequestered carbon per cubic meter of the aquifer.

4.2. Role of Geochemistry on CO_2 Trapping at Different Scales

In this subsection, the effect of geochemical interactions on solubility trapping and the total amount of sequestered carbon is studied at different time scales. Figure 3 shows the amount of solution trapping and total sequestered carbon versus dimensionless time for laboratory scale (Case 1) and field scale (Case 2) as well as the base case (no geochemistry). As it can be seen, rock-fluid interactions have different effects on the process over different time scales. For the laboratory scale (Case 1), the time scale is in days, and

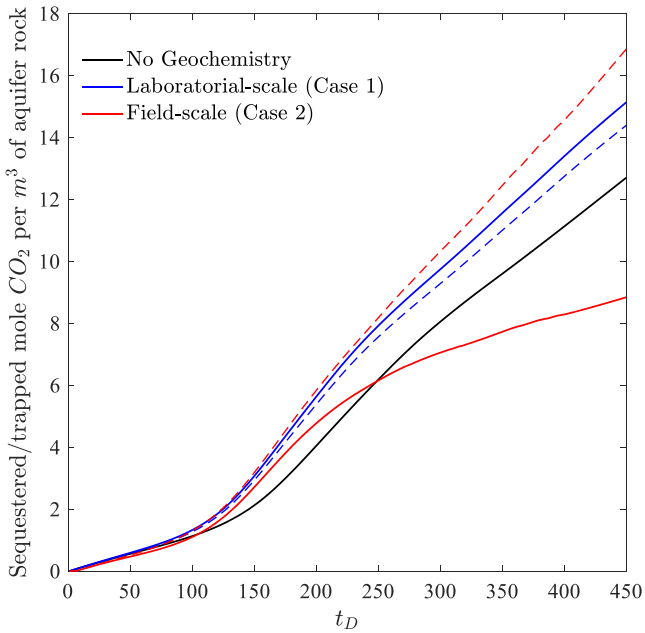

Figure 3. Amount of solubility trapping and the total sequestered carbon per cubic meter of the aquifer rock for nonreactive and the reactive cases (solid lines show solubility trapping, and dashed lines show total sequestered carbon).

the solution trapping is enhanced through rock-fluid interactions as the mineral dissolution outweighs the precipitation; notably, the total amount of carbon sequestration is still increased in comparison to the base case (no-geochemistry). On the other hand, for the field-scale case (Case 2), where the time scale is in the range of years, the solution trapping is weakened while the amount of total sequestered carbon is enhanced through precipitation of carbonate minerals.

Figure 4 depicts the amount of carbon mineralization for Cases 1 and 2. In Case 1 the amount of carbon precipitation is less than dolomite dissolution from the rock into the fluid. In this case, the aqueous phase becomes acidic, and the rock minerals dissolve into the aqueous phase. When each phase becomes supersaturated based on the local water composition, the precipitation takes place. In Case 1, dolomite, albite, and k-feldspar dissolve from the rock into the aqueous phase, while the main precipitating minerals are dawsonite, kaolinite, and magnesite. An interesting point is that in this condition, calcite does not precipitate as the time scale is not long enough to increase the water pH into calcite precipitation window. In this condition, the convective-diffusive mixing is improved due to rock dissolution into the aqueous phase, which increases local density in CO_2 fingers.

Based on the results of field-scale model (Case 2), carbon mineralization is greater than carbon dissolution. This phenomenon is not uniform throughout the process, and as it can be seen in Figure 4 in early times, the dolomite dissolution is more than carbonates precipitation. However, this trend changes, and after a critical time (~150 days), afterward, the mineralization outweighs carbon dissolution. In this case, calcite precipitation occurs in the model, and both dolomite precipitation and dissolution are seen in the results, but dolomite dissolution is more than dolomite precipitation. The most important precipitating carbonate minerals are dawsonite and magnesite. Consequently, the concentration of aluminum decreases in the swept area of the aquifer due to dawsonite and kaolinite precipitation. Also, the porosity of the aquifer decreases in this case, which happens mostly near the top boundary of the domain.

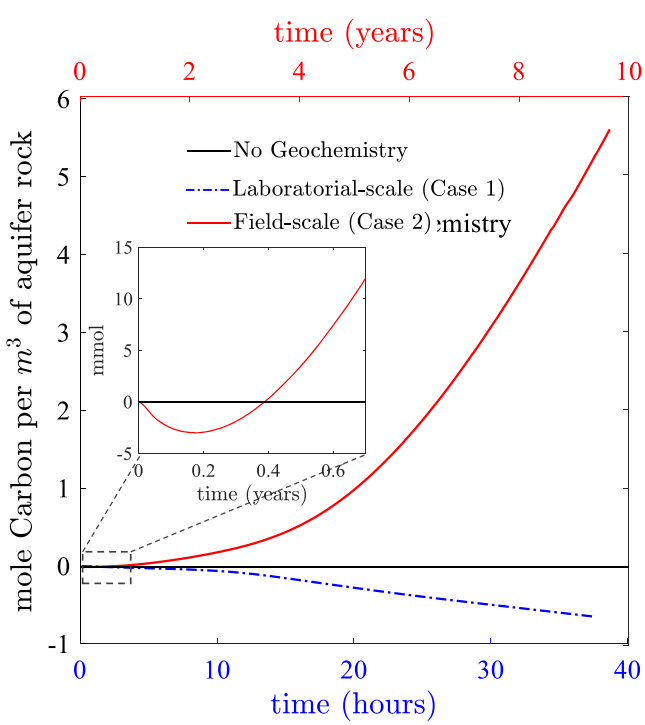

Figure 4. Amount of mineral trapping per cubic meter of aquifer rock for laboratorial scale (Case 1) and field scale (Case 2) (Note: Positive values show precipitation, and negative values are associated with dissolution).

An important result in terms of convective mixing is that, at the field scale, the local density of the aqueous phase is decreased due to the dominant mineral precipitation (mostly dawsonite, magnesite, and kaolinite), which hinders the finger propagation and convective mixing, while the overall carbon sequestration is enhanced (see Figure 4). This effect may shut down the convective-diffusive mixing in low Rayleigh numbers as experimentally shown by Cardoso and Andres (2014), which is discussed in section 4.3 in detail.

4.3. Carbon Trapping Mechanisms Under Geochemistry

This subsection studies the processes through which solubility trapping is affected by rock-fluid interaction in carbon sequestration in sandstone aquifers. Figure 5 shows the dimensionless carbon pseudo-component concentration for both Cases 1 and 2 for two different dimensionless times. Comparing Figures 5a and 5b with Figures 2a and 2b shows that at large scale, some small (weak) fingers are suppressed and, also, the formed fingers are narrower and have lower carbon concentration contrast (these phenomena are shown using red circles and white rectangles in Figure 5, respectively).

Figure 6a shows the cumulative amount of local carbon mineralization ($C_{\text{mineralized}}$), while Figure 6b shows the rate of carbon mineralization at $t_D = 360$ ($\frac{dC_{min.}}{dt_D}$), and Figure 6c shows the corresponding pH map of the

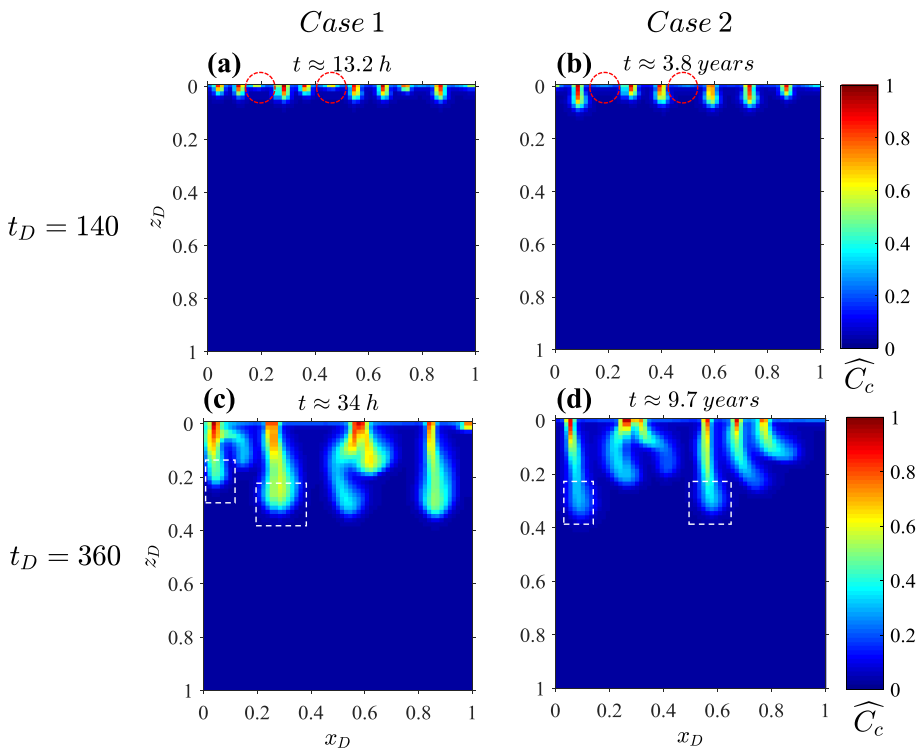

Figure 5. Dimensionless carbon pseudo-component concentration profile for two different time snapshots for (a and c) Case 1 and (b and d) Case 2. (Red circles and white rectangles show finger suppression and decreased carbon concentration contrast phenomena due to rock-fluid interactions, respectively).

simulation domain for Case 2. Due to low pH, the rate of carbon mineralization at the top of the aquifer is lower than the base of aquifer. Also, as shown in the snapshot, the rate of carbon mineralization is negative at the top layer, showing that the rate of dolomite dissolution is higher than dawsonite, magnesite, and calcite precipitation. Moreover, the highest rate of carbon mineralization is in the middle of the plume, where two conditions coexist: First, the pH is high enough to reach mineralization window, and second, the concentration of carbon bearing species is high enough to cause supersaturation of carbonate phases and trigger mineral precipitation (see equation (16)).

Activity/dissolution of primary minerals increases the pH and paves the way for carbonate precipitation and also enhances convective-diffusive mixing. In Case 1, the time scale is not long enough to increase the pH, as a result, the pH profile is significantly lower in Case 1 in comparison to Case 2, which leads to the domination of the dissolution process, as discussed before.

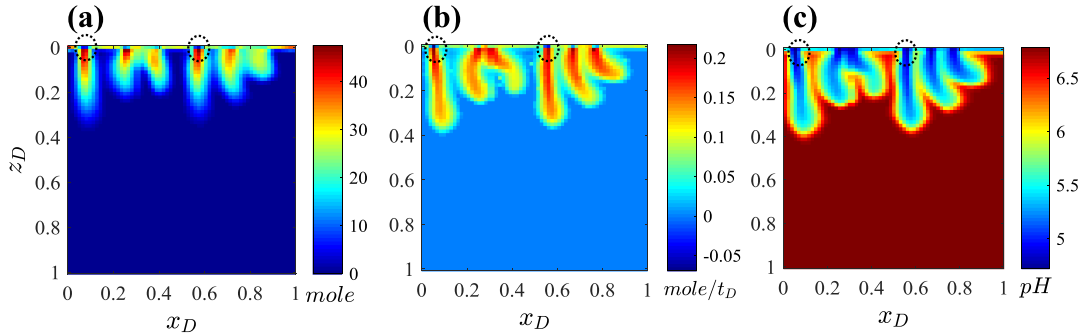

Figure 6. (a) Local cumulative amount of carbon mineralization ($C_{\text{mineralized}}$), (b) the rate of carbon mineralization, and (c) pH distribution for Case 2, $t_D = 360$ and $t \approx 9.7$ years. (Black circles show examples of the regions where the carbon mineralization rate is negative due to low pH.)

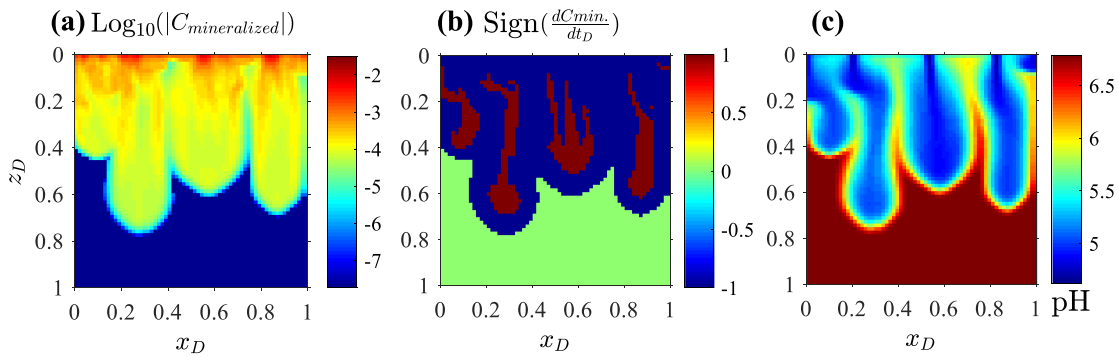

Figure 7. (a) Logarithm of absolute value of mineralized carbon ($\mathrm{Log}_{10}(|C_{\mathrm{mineralized}}|)$), (b) sign of the rate of carbon mineralization ($\mathrm{Sign}(\frac{dCmin.}{dt_D})$), and (c) pH map for Case 1, $t_D = 650$ and $t \approx 61$ hr. (Note: in (b) red color shows precipitation, and blue color shows dissolution)

Figure 7a shows the logarithm of absolute value of the local mineralized carbon for Case 1. As was discussed, for this case, dolomite dissolution is the dominant mechanism. Figure 7b shows the sign of the carbon mineralization rate as a way to distinguish dissolution/precipitation regions. Precipitation is the dominant mechanism in the middle of the fingers. At the edge of the fingers, dissolution is the dominant mechanism, which enhances finger propagation and convection mixing. In Case 2 (see Figure 6b) the precipitation is dominant in all regions of the plume, which diminishes the plume propagation.

Figure 8 shows the distribution of porosity after almost 10 years for Case 2. The greatest impairment due to carbonate and kaolinite precipitation happens in upper parts of the aquifer. In some grid blocks due to low pH, silicate and dolomite dissolution outweighs precipitation. For these regions, porosity increases (these parts are shown with black circles in Figure 8a, which is consistent with Figure 6). This porosity (and therefore permeability) improvement can help to increase CO_2 flux.

Figure 9 shows the pattern of dolomite dissolution/precipitation (Figure 9a) and horizontally averaged value of the precipitated mineral for magnesite, calcite, kaolinite, and dolomite (secondary minerals) (Figure 9b). As it is shown in Figure 9a, the dolomite reaction is not uniform throughout the simulation domain, and both dissolution and precipitation dominant regions coexist in the simulation domain. To clarify, dissolution is the dominant mechanism in the upper layers of the aquifer (where the pH is low; see Figure 6c) and in the edges of the fingers (where carbon pseudo-component concentration and, consequently, HCO_3^- concentration are low; see Figure 5d).

Based on Figure 9b, the most important precipitating carbonate mineral is dawsonite, which is in agreement with findings of other researchers (White et al., 2005; Wei et al., 2015; Xu et al., 2005).

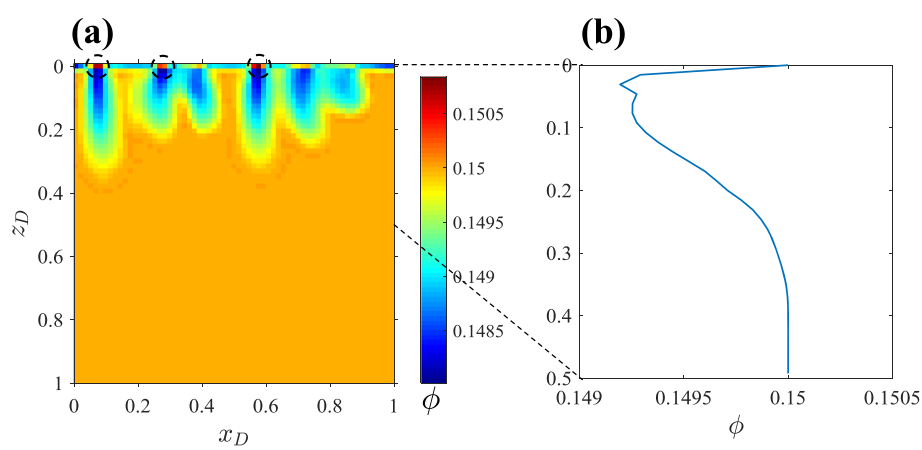

Figure 8. (a) Porosity distribution in Case 2 and (b) vertical averaged value of porosity versus dimensionless depth after 9.7 years. (Note: black circles show examples of dissolution dominant regions where porosity is increased.)

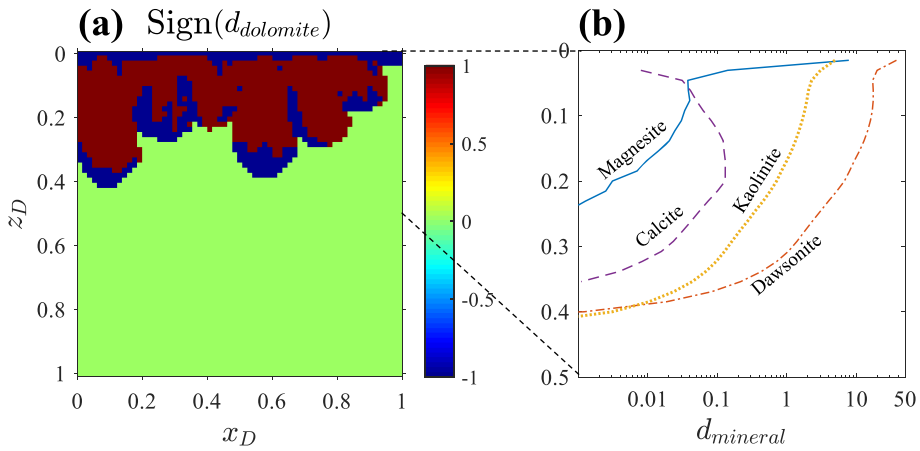

Figure 9. (a) Dolomite dissolution/precipitation pattern for Case 2 and (b) vertical averaged value of cumulative precipitation for dawsonite, kaolinite, calcite, and magnesite after 9.7 years (note: In (a) red and blue colors show precipitation and dissolution, respectively).

4.4. Reactive Convective-Diffusive Mixing at Different Rayleigh Numbers

Figure 10 demonstrates the effect of Rayleigh (Ra) number on CO_2 dissolution and reaction. Onset time (t_c), which defines the start of the convective-dominant regime has been shown in Figure 10a. Maximum finger penetration into the aquifer (Figure 10b) as well as the total amount of sequestered carbon per m^3 of aquifer rock (Figure 10c) are shown for different Rayleigh numbers ($1{,}500 < Ra < 55{,}000$) for both reactive and no-reaction scenarios. The Rayleigh number in these cases is controlled by changing the permeability of the aquifer (2.5×10^{-14} m$^2 \leq K \leq 80\times10^{-14}$ m^2), while all other simulation parameters are kept constant. Moreover, all simulations were performed on the field-scale model at 50 m × 50 m.

Based on Figure 10a, onset time of convection shows a clear relation with $\sim 1/Ra^n$ in both reactive and non-reactive cases while the exponent (n) is increased as a result of geochemical interactions. Therefore, the rock-fluid interactions stimulate the instabilities. The provided results are in-line with recent experimental (Rasmusson et al., 2017) and numerical (Amooie et al., 2018) studies, which suggest $t_c = \frac{1}{Ra^n}.\frac{H^2}{D_e}$ and calculated $n = 1.1427$ and $n = 1.14$, respectively. Figure 10b provides the downward movement of carbon concentration for a fixed time ($t = 4$ years) for different Rayleigh numbers. Interestingly, it shows that in diffusive regime, the geochemical interactions hinder carbon concentration propagation while in convective regime the rock-fluid interactions help the carbon species to go deeper in the aquifer. The mechanisms in both regimes were discussed in detail previously. Figure 10c depicts the total amount of sequestered carbon at a fixed time ($t = 4$ years) for different Rayleigh numbers. It shows that the geochemical interactions

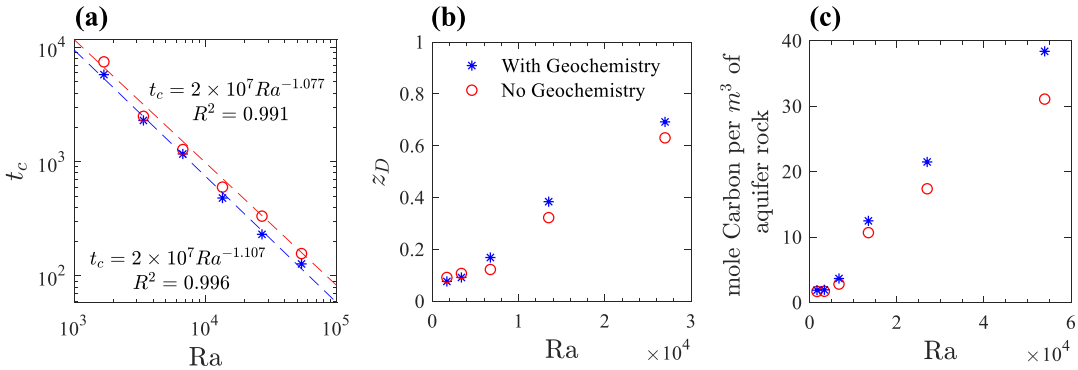

Figure 10. (a) Critical onset time (t_c, days) for different Rayleigh numbers (b) maximum penetration of carbon fingers versus dimensionless depth (z_D) after 4 years for different Rayleigh numbers and (c) the total amount of sequestered carbon per cubic meter of aquifer rock after 4 years for different Rayleigh numbers considering geochemical interactions and without geochemistry cases. The onset time was determined based on the deviation of dissolution rate from diffusion dominated region (note: Pay attention to logarithmic scales of x and y axes in (a)).

improve the carbon sequestration and its role is higher in higher Rayleigh numbers. In the convection dominant regime, the amount of total sequestered carbon seems to have a linear relation with Rayleigh number at a fixed time.

5. Summary and Conclusions

In this research a 2-D multicomponent reactive convective-diffusive formulation was presented. Realistic sandstone geochemistry was considered to study the effect of geochemistry on density-driven mixing process. Eight solid-phase kinetic reactions along with 10 aqueous-phase instantaneous (equilibrium) reactions were coupled with the flow equations using SNIA. The system was representative of underground conditions to study the effect of rock-fluid interactions on CO_2 density-driven mixing in sandstone aquifers.

Two different reactive cases at different length scales were successfully modeled using the developed reactive simulator. The cases were representative of the laboratory-scale and field-scale circumstances. The results showed that the effects of geochemistry in these scales were different due to different time scales of events. The results were also compared to no-reaction case to draw a conclusion about the effect of rock-fluid interactions from the simulation results.

The main conclusions are given as follows:

1. As the convection-diffusion process started, CO_2 diffused into the aquifer and decreased the pH of the aqueous phase. In acidic condition k-feldspar, albite, and dolomite dissolved, causing increase in aluminum and silicon components in the water. As the diffusion went on, the instability was enhanced, and later on, finger-shape concentration profiles were formed inside the domain, which enhanced CO_2 flux into the domain. By increasing total carbon content, supersaturation of carbonate minerals occurred, and as a result, dawsonite, magnesite, and calcite along with kaolinite clay precipitated, which caused carbon mineralization and porosity impairment in upper parts of the aquifer.
2. While mineralization hindered density-driven mixing due to decreasing aqueous-phase density, rock minerals dissolution enhanced dissolution trapping and mixing. These mechanisms had different extents at different scales. At the laboratory scale, the dissolution was dominant, while at the field scale, the precipitation was dominant. As a result, finger development was enhanced for the laboratory scale, while it was reduced for the field scale. At the field scale, finger suppression and weakening mechanism of the concentration contrast were illustrated by carbon pseudo-component concentration profile mapping in different time snapshots.
3. While geochemical interactions hindered density-driven mixing at the field scale, it improved total sequestered carbon through carbon mineralization in medium to high Rayleigh numbers. It was shown that at the field scale for project lifetime after almost 10 years, 28% of the total sequestered carbon was stored in the form of mineralized carbonates.
4. Dawsonite was the most important precipitating carbonate mineral in this study, while magnesite and calcite precipitation were also important. Out simulations results demonstrate that Dawsonite is a clay mineral containing aluminum and the aluminum interaction with carbon is important for improving the prediction of carbon mineralization. Noticeably even though dolomite dissolution outweighed its precipitation, dolomite precipitation also occurred in some parts of the aquifer that is the inner plume areas. In these regions, not only pH was high but also carbon pseudo-component concentration was high, resulting in dolomite saturation ratio to become less than 1. Due to carbon mineralization and kaolinite precipitation, porosity impairment happened mostly close to upper boundary of the aquifer, with the highest amount of 1.3% of the initial porosity after almost 10 years.
5. The effect of geochemistry in convective-diffusive flow was also studied for $1{,}500 < Ra < 55{,}000$. The geochemistry was found to stimulate the instability; as a result, the onset time is smaller when the rock-fluid interactions are taken into account. It was also found that the geochemistry helps the carbon fingers to propagate deeper in the aquifer in convection dominant flow regime and the effect is more significant in higher Rayleigh numbers.

Nomenclature

K_{eq}	equilibrium reaction constant
V_b	bulk volume $[m^3]$

V_m	molar volume $\left[\frac{m^3}{mol}\right]$
c	concentration $\left[\frac{mol}{kg_w}\right]$
D	diffusion coefficient $\left[\frac{m^2}{s}\right]$
g	gravity acceleration $\left[\frac{m}{s^2}\right]$
H	height [m]
K	permeability $\left[m^2\right]$
k	reaction rate constant
L	length [m]
m	number of moles
P	pressure [atm]
S	sink/source term due to geochemical interactions $\left[\frac{mol/kg_w}{s}\right]$
T	temperature [Kelvin]
t	time [s]
u	velocity $\left[\frac{m}{s}\right]$

Abbreviations

CCS	carbon capture and storage
DFT	discrete Fourier transform
FTCS	forward-time central-space
IAP	ionic activity product
np	number of pseudo-components
Ra	Rayleigh number
SC	supercritical
SNIA	sequential noniterative approach

Subscripts

0	initial
c	carbon pseudo-component
D	dimensionless
ps	pseudo-component
r	reference
x	x direction
z	z direction

Superscripts

n_1, n_2, m	reaction rate exponent constants
*	dimensionless
t	time

Greek Letters

β	coefficient of density increase by concentration $\left[\frac{kg}{mol/lit}\right]$
χ	aspect ratio
μ	viscosity [atm.s]
Ω	saturation ratio
ϕ	porosity
ψ	stream function $\left[\frac{m^3}{m.s}\right]$
ρ	density $\left[\frac{kg}{m^3}\right]$

Notations

$\mathscr{A}$	surface area $\left[m^2\right]$
$\widehat{\ }$	pseudo-component
{ }	activity

Data Availability Statement

Data sets related to this article can be found at DOI: 10.17632/m2dhzjdhdr.1, an open-source online data repository hosted at Mendeley Data.

Acknowledgments
The authors would like to thank Prof. Michael Celia from Princeton University for his fruitful comments. The authors would also like to acknowledge the University of Manchester for providing the PhD funding for Hamidreza Erfani through President's Doctoral Scholarship (PDS) award.

References

Agartan, E., Trevisan, L., Cihan, A., Birkholzer, J., Zhou, Q., & Illangasekare, T. H. (2015). Experimental study on effects of geologic heterogeneity in enhancing dissolution trapping of supercritical CO2. *Water Resources Research*, *51*, 1635–1648. https://doi.org/10.1002/2014WR015778

Amin, S. M., Weiss, D., & Blunt, M. (2014). Reactive transport modelling of geologic CO2 sequestration in saline aquifers: The influence of pure CO2 and of mixtures of CO2 with CH4 on the sealing capacity of cap rock at 37 C and 100 bar. *Chemical Geology*, *367*, 39–50.

Aminu, M. D., Nabavi, S. A., Rochelle, C. A., & Manovic, V. (2017). A review of developments in carbon dioxide storage. *Applied Energy*, *208*, 1389–1419.

Amooie, M. A., Soltanian, M. R., & Moortgat, J. (2018). Solutal convection in porous media: Comparison between boundary conditions of constant concentration and constant flux. arXiv preprint arXiv:1809.02212.

Audigane, P., Gaus, I., Czernichowski-Lauriol, I., Pruess, K., & Xu, T. (2007). Two-dimensional reactive transport modeling of CO2 injection in a saline aquifer at the Sleipner site, North Sea. *American journal of science*, *307*(7), 974–1008.

Babaei, M., & Islam, A. (2018). Convective-reactive CO2 dissolution in aquifers with mass transfer with immobile water. *Water Resources Research*, *54*, 9585–9604. https://doi.org/10.1029/2018WR023150

Bakhshi, P., Kharrat, R., Hashemi, A., & Zallaghi, M. (2018). Experimental evaluation of carbonated waterflooding: A practical process for enhanced oil recovery and geological CO2 storage. *Greenhouse Gases: Science and Technology*, *8*(2), 238–256.

Balashov, V. N., Guthrie, G. D., Hakala, J. A., Lopano, C. L., Rimstidt, J. D., & Brantley, S. L. (2013). Predictive modeling of CO2 sequestration in deep saline sandstone reservoirs: Impacts of geochemical kinetics. *Applied Geochemistry*, *30*, 41–56.

Barry, D., Bajracharya, K., Crapper, M., Prommer, H., & Cunningham, C. (2000). Comparison of split-operator methods for solving coupled chemical non-equilibrium reaction/groundwater transport models. *Mathematics and Computers in Simulation*, *53*(1-2), 113–127.

Blanc, P., Lassin, A., Piantone, P., Azaroual, M., Jacquemet, N., Fabbri, A., & Gaucher, E. C. (2012). Thermoddem: A geochemical database focused on low temperature water/rock interactions and waste materials. *Applied Geochemistry*, *27*(10), 2107–2116.

Bui, M., Adjiman, C. S., Bardow, A., Anthony, E. J., Boston, A., Brown, S., et al. (2018). Carbon capture and storage (CCS): The way forward. *Energy & Environmental Science*, *11*(5), 1062–1176.

Cardoso, S. S. S., & Andres, J. T. H. (2014). Geochemistry of silicate-rich rocks can curtail spreading of carbon dioxide in subsurface aquifers. *Nature communications*, *5*, 5743.

Carrayrou, J., Mose, R., & Behra, P. (2004). Operator-splitting procedures for reactive transport and comparison of mass balance errors. *Journal of Contaminant Hydrology*, *68*(3-4), 239–268.

Celia, M. A. (2017). Geological storage of captured carbon dioxide as a large-scale carbon mitigation option. *Water Resources Research*, *53*, 3527–3533. https://doi.org/10.1002/2017WR020841

Charlton, S. R., & Parkhurst, D. L. (2011). Modules based on the geochemical model PHREEQC for use in scripting and programming languages. *Computers & Geosciences*, *37*(10), 1653–1663.

Chevalier, S., Faisal, T. F., Bernabe, Y., Juanes, R., & Sassi, M. (2015). Numerical sensitivity analysis of density driven CO2 convection with respect to different modeling and boundary conditions. *Heat and Mass Transfer*, *51*(7), 941–952.

Cinar, Y., Riaz, A., & Tchelepi, H. A. (2007). Experimental study of CO2 injection into saline formations. In *SPE Annual Technical Conference and Exhibition*, Society of Petroleum Engineers.

Cooley, J. W., Lewis, P., & Welch, P. (1970). The fast Fourier transform algorithm: Programming considerations in the calculation of sine, cosine and Laplace transforms. *Journal of Sound and Vibration*, *12*(3), 315–337.

Cussler, E. L. (2009). *Diffusion: Mass transfer in fluid systems*. Cambridge: Cambridge university press.

De Simoni, M., Sanchez-Vila, X., Carrera, J., & Saaltink, M. W. (2007). A mixing ratios-based formulation for multicomponent reactive transport. *Water Resources Research*, *43*, W07419. https://doi.org/10.1029/2006WR005256

Edwards, R. W. J., Celia, M. A., Bandilla, K. W., Doster, F., & Kanno, C. M. (2015). A model to estimate carbon dioxide injectivity and storage capacity for geological sequestration in shale gas wells. *Environmental science & technology*, *49*(15), 9222–9229.

Emami-Meybodi, H., & Hassanzadeh, H. (2015). Two-phase convective mixing under a buoyant plume of CO2 in deep saline aquifers. *Advances in water resources*, *76*, 55–71.

Emami-Meybodi, H., Hassanzadeh, H., Green, C. P., & Ennis-King, J. (2015). Convective dissolution of CO2 in saline aquifers: Progress in modeling and experiments. *International Journal of Greenhouse Gas Control*, *40*, 238–266.

Ennis-King, J. P., & Paterson, L. (2005). Role of convective mixing in the long-term storage of carbon dioxide in deep saline formations. *Society of Petroleum Engineers Journal*, *10*(03), 349–356.

Ennis-King, J., & Paterson, L. (2007). Coupling of geochemical reactions and convective mixing in the long-term geological storage of carbon dioxide. *International Journal of Greenhouse Gas Control*, *1*(1), 86–93.

Erfani, H., Joekar-Niasar, V., & Farajzadeh, R. (2019). Impact of microheterogeneity on upscaling reactive transport in geothermal energy. *ACS Earth and Space Chemistry*, *3*, 2045–2057.

Farajzadeh, R., Matsuura, T., van Batenburg, D., & Dijk, H. (2012). Detailed modeling of the alkali/surfactant/polymer (ASP) process by coupling a multipurpose reservoir simulator to the chemistry package PHREEQC. *SPE Reservoir Evaluation & Engineering*, *15*(04), 423–435.

Farajzadeh, R., Salimi, H., Zitha, P. L. J., & Bruining, H. (2007). Numerical simulation of density-driven natural convection in porous media with application for CO2 injection projects. *International Journal of Heat and Mass Transfer*, *50*(25-26), 5054–5064.

Fu, X., Cueto-Felgueroso, L., Bolster, D., & Juanes, R. (2015). Rock dissolution patterns and geochemical shutdown of CO2-brine-carbonate reactions during convective mixing in porous media. *Journal of Fluid Mechanics*, *764*, 296–315.

Gaus, I. (2010). Role and impact of CO2–rock interactions during CO2 storage in sedimentary rocks. *International journal of greenhouse gas control*, *4*(1), 73–89.

Gaus, I., Azaroual, M., & Czernichowski-Lauriol, I. (2005). Reactive transport modelling of the impact of CO2 injection on the clayey cap rock at Sleipner (North Sea). *Chemical Geology*, *217*(3-4), 319–337.

Ghesmat, K., Hassanzadeh, H., & Abedi, J. (2011). The impact of geochemistry on convective mixing in a gravitationally unstable diffusive boundary layer in porous media: CO 2 storage in saline aquifers. *Journal of Fluid Mechanics*, *673*, 480–512.

Godec, M., Kuuskraa, V., Van Leeuwen, T., Melzer, L. S., & Wildgust, N. (2011). CO2 storage in depleted oil fields: The worldwide potential for carbon dioxide enhanced oil recovery. *Energy Procedia*, *4*, 2162–2169.

Hassanzadeh, H., Pooladi-Darvish, M., & Keith, D. W. (2005). Modelling of convective mixing in co storage. *Journal of Canadian Petroleum Technology*, *44*(10), 43–51.

Hassanzadeh, H., Pooladi-Darvish, M., & Keith, D. W. (2007). Scaling behavior of convective mixing, with application to geological storage of CO2. *AIChE journal*, *53*(5), 1121–1131.

Haszeldine, R. S. (2009). Carbon capture and storage: how green can black be? *Science*, *325*(5948), 1647–1652.

Hellevang, H., Pham, V. T. H., & Aagaard, P. (2013). Kinetic modelling of CO2-water-rock interactions. *International Journal of Greenhouse Gas Control*, *15*, 3–15.

Hidalgo, J. J., & Carrera, J. (2009). Effect of dispersion on the onset of convection during CO2 sequestration. *Journal of Fluid Mechanics*, *640*, 441–452.

Hidalgo, J. J., Dentz, M., Cabeza, Y., & Carrera, J. (2015). Dissolution patterns and mixing dynamics in unstable reactive flow. *Geophysical Research Letters*, *42*, 6357–6364. https://doi.org/10.1002/2015GL065036

Islam, A. W., Sharif, M. A., & Carlson, E. S. (2013). Numerical investigation of double diffusive natural convection of CO2 in a brine saturated geothermal reservoir. *Geothermics*, *48*, 101–111.

Islam, A., Sun, A. Y., & Yang, C. (2016). Reactive transport modeling of the enhancement of density-driven CO2 convective mixing in carbonate aquifers and its potential implication on geological carbon sequestration. *Scientific reports*, *6*, 24768.

Joekar-Niasar, V., Doster, F., Armstrong, R. T., Wildenschild, D., & Celia, M. A. (2013). Trapping and hysteresis in two-phase flow in porous media: A pore-network study. *Water Resources Research*, *49*, 4244–4256. https://doi.org/10.1002/wrcr.20313

Judith, B. (2017). *The Paris Agreement*. Cham, Switzerland: Springer International Publishing.

Kampman, N., Bickle, M., Wigley, M., & Dubacq, B. (2014). Fluid flow and CO2-fluid-mineral interactions during CO2-storage in sedimentary basins. *Chemical Geology*, *369*, 22–50.

Kanney, J. F., Miller, C. T., & Kelley, C. T. (2003). Convergence of iterative split-operator approaches for approximating nonlinear reactive transport problems. *Advances in Water Resources*, *26*(3), 247–261.

Knauss, K. G., Johnson, J. W., & Steefel, C. I. (2005). Evaluation of the impact of CO2, co-contaminant gas, aqueous fluid and reservoir rock interactions on the geologic sequestration of CO2. *Chemical geology*, *217*(3-4), 339–350.

Kolster, C., Masnadi, M. S., Krevor, S., Mac Dowell, N., & Brandt, A. R. (2017). CO 2 enhanced oil recovery: A catalyst for gigatonne-scale carbon capture and storage deployment? *Energy & Environmental Science*, *10*(12), 2594–2608.

Koytsoumpa, E. I., Bergins, C., & Kakaras, E. (2017). The CO2 economy: Review of CO2 capture and reuse technologies. *The Journal of Supercritical Fluids*, *132*, 3–16.

Kurtz, L., Smith, R., Parks, C., & Boney, L. (1978). A comparison of the method of lines to finite difference techniques in solving time-dependent partial differential equations. *Computers & Fluids*, *6*(2), 49–70.

Laidler, K. J. (1984). The development of the Arrhenius equation. *Journal of Chemical Education*, *61*(6), 494.

Lasaga, A. C. (2014). *Kinetic theory in the Earth sciences* (Vol. 402). Princeton: Princeton university press.

Li, L., Peters, C. A., & Celia, M. A. (2006). Upscaling geochemical reaction rates using pore-scale network modeling. *Advances in water resources*, *29*(9), 1351–1370.

Liu, F., Lu, P., Zhu, C., & Xiao, Y. (2011). Coupled reactive flow and transport modeling of CO2 sequestration in the Mt. Simon sandstone formation, Midwest USA. *International Journal of Greenhouse Gas Control*, *5*(2), 294–307.

Loodts, V., Knaepen, B., Rongy, L., & De Wit, A. (2017). Enhanced steady-state dissolution flux in reactive convective dissolution. *Physical Chemistry Chemical Physics*, *19*(28), 18,565–18,579.

Majumdar, A., & Deutch, J. (2018). Research opportunities for CO2 utilization and negative emissions at the Gigatonne Scale. *Joule*, *2*(5), 805–809.

Meybodi, H. E., & Hassanzadeh, H. (2013). Stability analysis of two-phase buoyancy-driven flow in the presence of a capillary transition zone. *Physical Review E*, *87*(3), 33009.

Moghaddam, R. N., Rostami, B., Pourafshary, P., & Fallahzadeh, Y. (2012). Quantification of density-driven natural convection for dissolution mechanism in CO2 sequestration. *Transport in porous media*, *92*(2), 439–456.

Multiphysics, & COMSOL (2012). Comsol multiphysics user guide (version 4.3 a). COMSOL, AB, pp. 39–40.

Nardi, A., Idiart, A., Trinchero, P., de Vries, L. M., & Molinero, J. (2014). Interface COMSOL-PHREEQC (iCP), an efficient numerical framework for the solution of coupled multiphysics and geochemistry. *Computers & Geosciences*, *69*, 10–21.

Nield, D. A., & Bejan, A. (2006). *Convection in porous media*, vol. 3. United States: Springer.

Oreskes, N. (2004). The scientific consensus on climate change. *Science*, *306*(5702), 1686–1686.

Orr Jr, F. M. (2009). CO2 capture and storage: Are we ready? *Energy & Environmental Science*, *2*(5), 449–458.

Orr Jr, F. M. (2018). Carbon capture, utilization, and storage: An update. *SPE Journal*, *23*(06), 2–444.

Palandri, J. L., & Kharaka, Y. K. (2004). A compilation of rate parameters of water-mineral interaction kinetics for application to geochemical modeling. Geological Survey Menlo Park CA.

Parkhurst, D. L., & Appelo, C. A. J. (1999). User's guide to PHREEQC (Version 2): A computer program for speciation, batch-reaction, one-dimensional transport, and inverse geochemical calculations. US Geological Survey Denver, CO.

Parkhurst, D. L., & Wissmeier, L. (2015). PhreeqcRM: A reaction module for transport simulators based on the geochemical model PHREEQC. *Advances in water resources*, *83*, 176–189.

Rasmusson, M., Fagerlund, F., Rasmusson, K., Tsang, Y., & Niemi, A. (2017). Refractive-light-transmission technique applied to density-driven convective mixing in porous media with implications for geological CO2 storage. *Water Resources Research*, *53*, 8760–8780. https://doi.org/10.1002/2017WR020730

Rockström, J., Schellnhuber, H. J., Hoskins, B., Ramanathan, V., Schlosser, P., Brasseur, G. P., et al. (2016). The world's biggest gamble. *Earth's Future*, *4*(10), 465–470.

Rogelj, J., Den Elzen, M., Höhne, N., Fransen, T., Fekete, H., Winkler, H., et al. (2016). Paris Agreement climate proposals need a boost to keep warming well below 2 C. *Nature*, *534*(7609), 631.

Sainz-Garcia, A., Abarca, E., Nardi, A., Grandia, F., & Oelkers, E. H. (2017). Convective mixing fingers and chemistry interaction in carbon storage. *International Journal of Greenhouse Gas Control*, *58*, 52–61.

Sathaye, K. J., Hesse, M. A., Cassidy, M., & Stockli, D. F. (2014). Constraints on the magnitude and rate of CO2 dissolution at Bravo Dome natural gas field. *Proceedings of the National Academy of Sciences*, *111*(43), 15,332–15,337.

Schumann, U., & Sweet, R. A. (1988). Fast Fourier transforms for direct solution of Poisson's equation with staggered boundary conditions. *Journal of Computational Physics*, *75*(1), 123–137.

Shokri, A., Mohammad, J., Bahaloo Horeh, M., Rostami, B., & Norouzi, H. (2018). Laboratory investigation of oil viscosity effect during carbonated water injection: Comparison of secondary and tertiary recovery. *The Canadian Journal of Chemical Engineering*, *96*(8), 1805–1813.

Soltanian, M. R., Amooie, M. A., Gershenzon, N., Dai, Z., Ritzi, R., Xiong, F., et al. (2017). Dissolution trapping of carbon dioxide in heterogeneous aquifers. *Environmental Science & Technology*, *51*(13), 7732–7741.

Soltanian, M. R., Hajirezaie, S., Hosseini, S. A., Dashtian, H., Amooie, M. A., Meyal, A., et al. (2019). Multicomponent reactive transport of carbon dioxide in fluvial heterogeneous aquifers. *Journal of Natural Gas Science and Engineering*, *65*, 212–223.

Tapia, J. F. D., Lee, J.-Y., Ooi, R. E., Foo, D. C., & Tan, R. R. (2016). Optimal CO2 allocation and scheduling in enhanced oil recovery (EOR) operations. *Applied energy*, *184*, 337–345.

Wei, N., Li, X., Wang, Y., Zhu, Q., Liu, S., Liu, N., & Su, X. (2015). Geochemical impact of aquifer storage for impure CO2 containing O2 and N2: Tongliao field experiment. *Applied energy*, *145*, 198–210.

White, S. P., Allis, R. G., Moore, J., Chidsey, T., Morgan, C., Gwynn, W., & Adams, M. (2005). Simulation of reactive transport of injected CO2 on the Colorado Plateau, Utah, USA. *Chemical geology*, *217*(3-4), 387–405.

Xu, T., Apps, J. A., & Pruess, K. (2005). Mineral sequestration of carbon dioxide in a sandstone-shale system. *Chemical geology*, *217*(3-4), 295–318.

Xu, P., & Yu, B. (2008). Developing a new form of permeability and Kozeny-Carman constant for homogeneous porous media by means of fractal geometry. *Advances in water resources*, *31*(1), 74–81.

Yang, C., Treviño, R. H., Hovorka, S. D., & Delgado-Alonso, J. (2015). Semi-analytical approach to reactive transport of CO2 leakage into aquifers at carbon sequestration sites. *Greenhouse Gases: Science and Technology*, *5*(6), 786–801.